Electronic Supplementary Information

for

Interfacial engineering for metal oxides/nitrides nano-heterojunctions towards high-rate lithium-ion storage

Bobo Zou,[‡a] Wei Zhang,[‡a] Yingxue Cui,[‡a] Sheng Li,[a] Guochun Li,[a] Xianhu Liu,[b] Dickon H. L. Ng,[c] Jingxia Qiu[a] and Jiabiao Lian*[a]

[a] Institute for Energy Research, Jiangsu University, Zhenjiang, 212013, China

[b] Key Laboratory of Materials Processing & Mold (Zhengzhou University), Ministry of Education, Zhengzhou University, Zhengzhou, 450002, China

[c] Department of Physics, The Chinese University of Hong Kong, Shatin, Hong Kong, China.

* Corresponding author: Tel/Fax: 0086-511-88799500. *E-mail address*: jblian@ujs.edu.cn.

[‡] These authors contributed equally to this work.

Material Characterizations. The phase structure and component of samples were investigated by a powder X-ray diffractometer (XRD, German Bruker D8 diffractometer with Cu Kα radiation, λ = 0.154 nm) and X-ray photoelectron spectroscopy (an ESCALAB 250Xi system, Thermo Scientific, with a monochromated Al K*α* X-ray source, 1486.6 eV). The morphology of samples was observed by a field emission scanning electron microscope (FE-SEM, JEOLJSM-7800F). High-resolution transmission electron microscope (HRTEM) images, selected area electron diffraction (SAED) patterns, and elemental mapping images were obtained on an FEI Tecnai G^2 F30 S-Twin TEM equipped with an energy dispersive X-ray (EDX) microanalyzer and operated at 300 kV.

Electrochemical Measurements. To evaluate the electrochemical performance of the as-prepared samples, the coin cells (CR 2032) with working electrode and Li foil (counter/reference electrode) were assembled in a glovebox (H_2O and O_2 concentrations below 1.0 ppm), using 1 M $LiPF_6$ in a 1:1 (V/V) mixture of ethylene carbonate (EC) and dimethyl carbonate (DMC) as an electrolyte, and a porous polypropylene membrane (Celgard 2400) as the separator. The working electrode consisted of the active materials, super conductive carbon black and polyvinylidene fluoride with the mass ratio of 8:1:1, respectively. The homogeneous slurry using N-methyl-2-pyrrolidone as solvent was spread onto a copper foil uniformly and dried in vacuum at 80 °C for 12 h. The mass loading of active material was about 1.0–1.2 mg/cm^2. All batteries should be aged at room temperature for 12 h to guarantee the good contact of electrode and electrolyte. Galvanostatic charge/discharge (GCD) tests were conducted on a Land battery test system in a potential window of 0.01–3.0 V at room temperature. Cyclic voltammetry (CV) at various scan rates and electrochemical impedance spectroscopy (EIS) measurements in the frequency range

from 100 kHz to 0.01 Hz were performed in the range of 0.01–3.0 V using an electrochemical work station (Gamry1000E).

Computational Methods and Calculation Detials. In the calculations, the Vienna ab initio Simulation Package (VASP) code[1,2] with electron correlation treated within the generalized gradient approximation (GGA)[3] using the Perdew-Burke-Ernzerhof (PBE)[4,5] exchange-correlation functional was applied. The projector-augmented-wave (PAW) pseudo-potentials[6] were chosen to describe ionic cores. The cutoff energy of 500 eV was adopted after a series of testing. Gaussian smearing of 0.02 eV to the orbital occupation was applied for the geometry optimization, and total energy computations with a tetrahedron method with Blöchl corrections were employed for accurate electronic structure calculations. The convergence threshold for the iteration in self-consistent-field (SCF) was set to be 10^{-5} eV, and for geometry optimizations by using the BFGS algorithm was set to be 0.01 eV/Å on the maximum force component. The long-range van der Waals (vdW) interactions were described by using the DFT-D3 method with Becke-Johnson damping.[1,2] The k-point sampling of the Brillouin zone was obtained using a 2 × 2 × 1 grid in the Monkhorst-Pack Scheme. Magnetic Fe atoms required electron localization. However, the PBE exchange-correlation functional had the tendency to delocalize unpaired electrons. In order to overcome this problem, all our calculations were done by the DFT+U method.[3] It was generally recognized that the localized 3d electrons correlation for Fe atom could be corrected by considering on-site Coulomb and exchange interactions. Based on the rotationally invariant approach, the corresponding U value was 3.29 for the Fe atom.

In our calculations, the most stable contact geometries of Fe_3O_4/Fe_2N nano-heterojunctions were obtained by optimizing the Fe_3O_4 (200) and Fe_2N (002) configurations. To simulate the

interface of Fe_3O_4(200)/Fe_2N (002), a rectangular cell of 23.945 Å × 8.388 Å was constructed by well matching a 5√3 × 3 unit cell of two-layer Fe_2N (002) (23.945 Å × 8.295 Å) with a 4 × 1 unit cell of two-layer Fe_3O_4 (200) (23.78 Å × 8.388 Å). A large vacuum slab of 20 Å was inserted in the z direction for surface isolation to prevent interaction between two neighboring surfaces.

The lithium storage properties of Fe_3O_4/Fe_2N nano-heterojunctions and Fe_2O_3 were evaluated by the adsorption strength of lithium. The adsorption energy of lithium was calculated with the equation:

$$E_{ads} = E_{total} - E_{heter}/E_{Fe2O3} - E_{Li} \qquad (1)$$

where, E_{heter} and E_{Fe2O3} are the energy of the Fe_3O_4/Fe_2N nano-heterojunctions and Fe_2O_3, respectively. E_{Li} is the energy of one lithium atom in the bulk stable crystal phase, and E_{total} is the total energy of the electrode system with lithium.

The climbing-image nudged elastic band (NEB) method [4,5] was used to map out the minimum energy path (MEP) and located the transition state for lithium-ion migration. At least seven intermediate images were interpolated between start point and end point in the interface of the Fe_3O_4/Fe_2N nano-heterojunctions. The transition state of the minimum energy pathway was confirmed by vibrational frequency calculations yielding a single imaginary frequency along the reaction coordinate.[6] The barrier height E_b was calculated as:

$$E_b = E^{TS} - E^{RS} \qquad (2)$$

where E^{TS} and E^{RS} are the total energies of the transition state and the connection to its equilibrated start point complex system, respectively.

REFERENCES

1. S. Grimme, J. Antony, S. Ehrlich and H. Krieg, *J. Chem. Phys.*, 2010, **132**, 154104.

2. S. Grimme, S. Ehrlich and L. Goerigk, *J. Comput. Chem.*, 2011, **32**, 1456.

3. S. L. Dudarev, G. A. Botton, S. Y. Savrasov, C. J. Humphreys and A. P. Sutton, A. *Phys. Rev. B*, 1998, **57**, 1505.

4. G. Henkelman, B. P. Uberuaga and H. Jónsson, *J. Chem. Phys.*, 2000, **113**, 9901.

5. G. Henkelman and H. Jónsson, *J. Chem. Phys.*, 2000, **113**, 9978.

6. J. Greeley and M. Mavrikakis, *Surf. Sci.,* 2003, **540**, 215.

Fig. S1 FE-SEM, TEM, and HRTEM images of the as-prepared α-Fe_2O_3 (a–c) and Fe_2N (d–f), respectively.

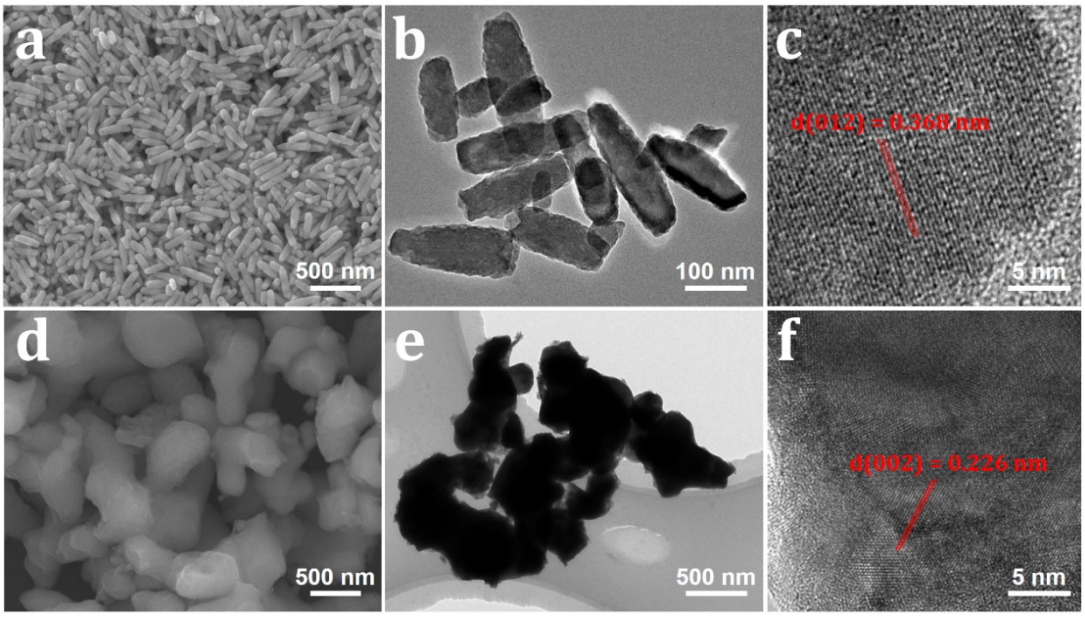

Fig. S2 FE-SEM, TEM, and HRTEM images of the as-prepared Nb_2O_5 (a–d), $Nb_{12}O_{29}/Nb_4N_5$-15 (e–h), and Nb_4N_5 (i–l), respectively.

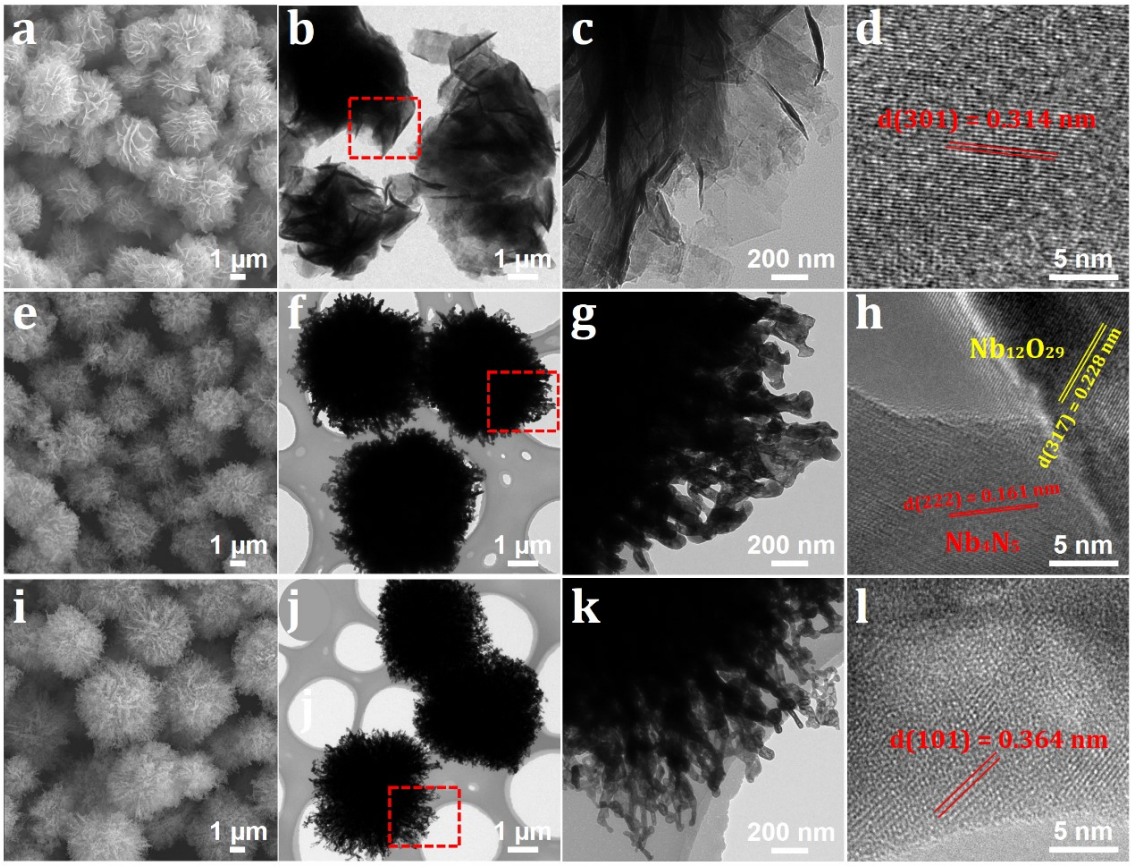

Fig. S3 FE-SEM images of the as-prepared WO_3 (a, b), $WO_{2.92}$/WN-15 (c, d), $WO_{2.92}$/ WN-30 (e, f), and WN (g, h).

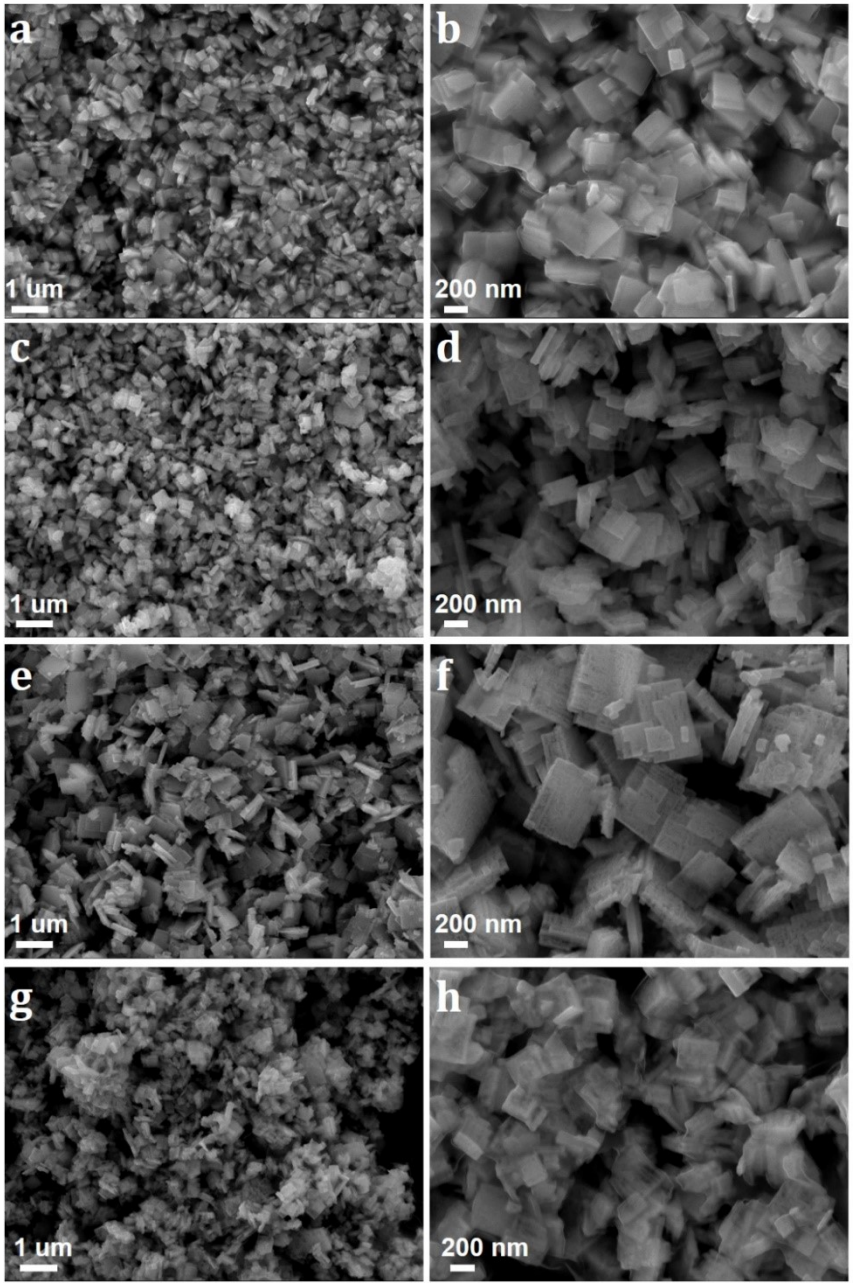

Fig. S4 Structural characterizations of Nb-based samples. (a) XRD patterns. High-resolution XPS spectra of Nb 3d (b), O 1s (c), and N 1s (d).

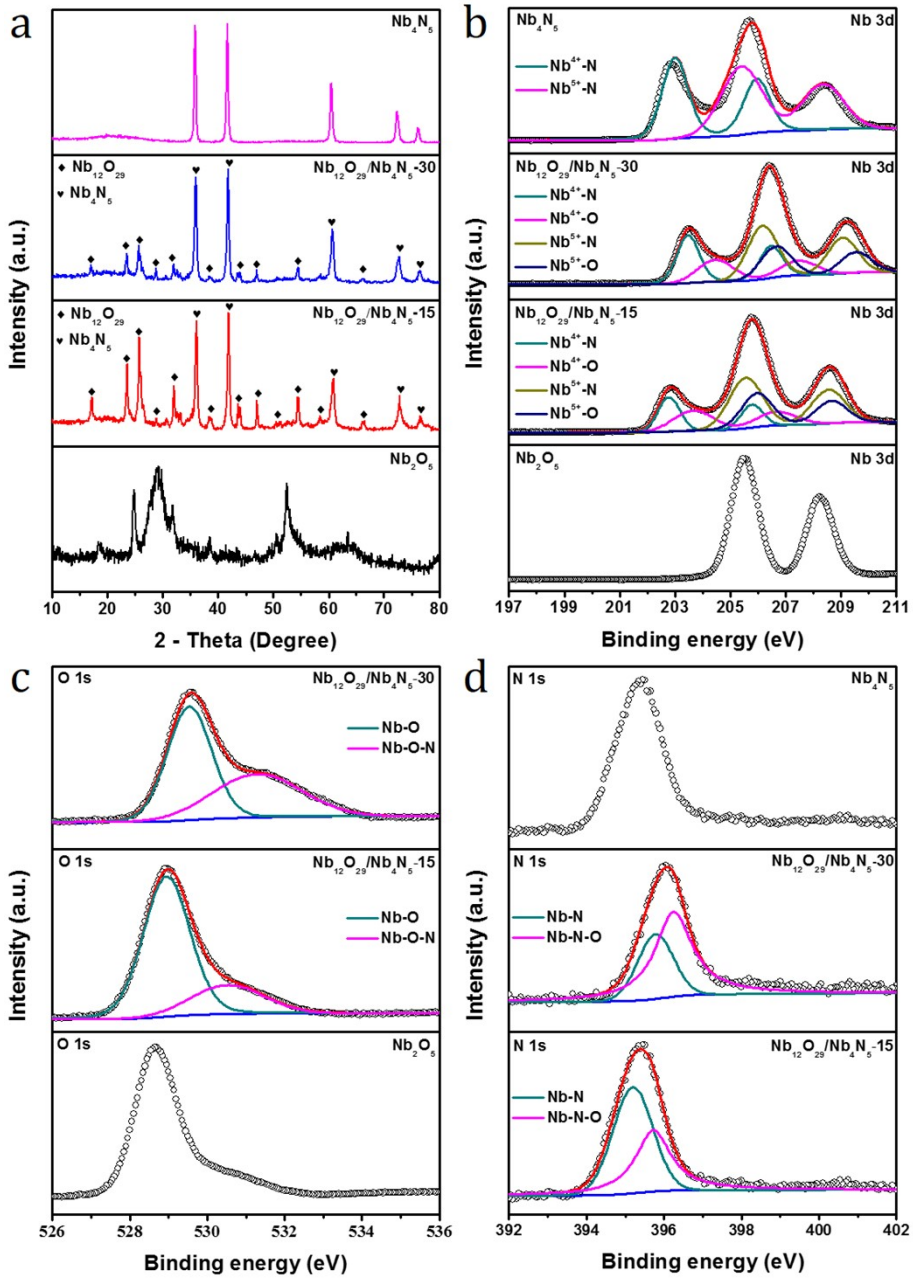

Fig. S5 XRD patterns of W-based samples.

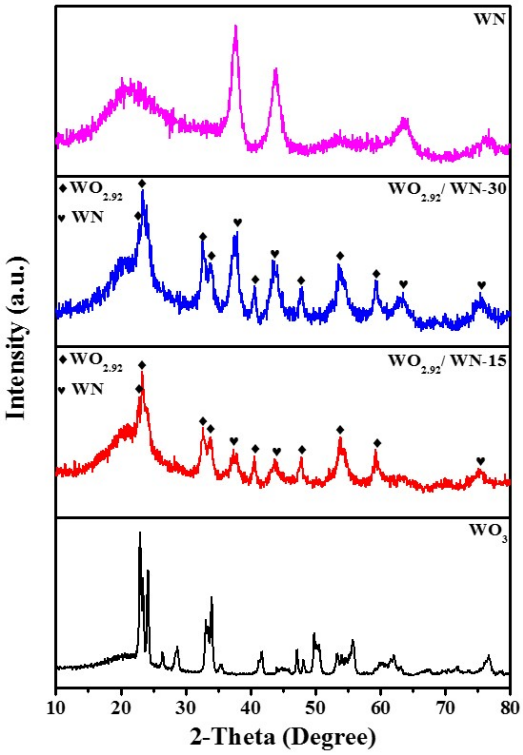

Table S1 The content of metal nitrides in their corresponding nano-heterojunctions.

Samples	**Fe_3O_4/Fe_2N-30**	**Fe_3O_4/Fe_2N-60**
W_{Fe2N}	12.32 %	24.77 %
Samples	**$Nb_{12}O_{29}/Nb_4N_5$-15**	**$Nb_{12}O_{29}/Nb_4N_5$-30**
W_{Nb4N5}	26.49 %	43.42 %
Samples	**$WO_{2.92}$/WN-15**	**$WO_{2.92}$/WN-30**
W_{WN}	5.34 %	9.68 %

Fig. S6 Schematic models to illustrate the lattice matching between Fe_3O_4 and Fe_2N.

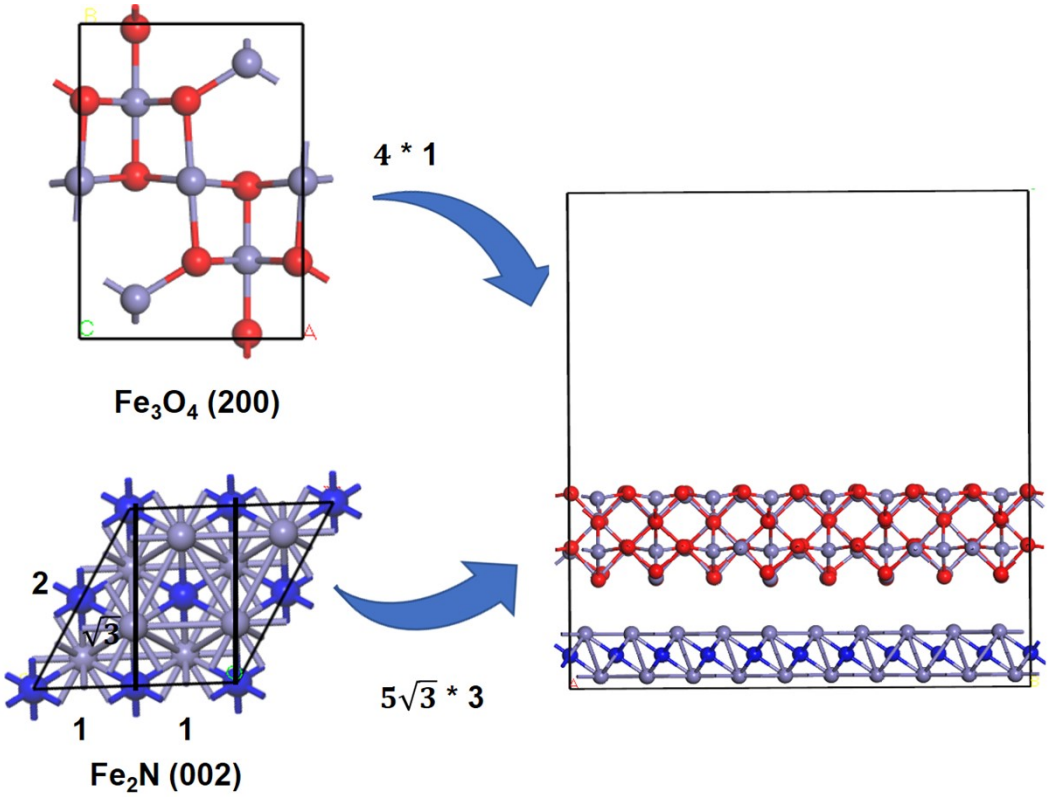

Fig. S7 The electron localization function of the Fe_3O_4/Fe_2N nano-heterojunctions system.

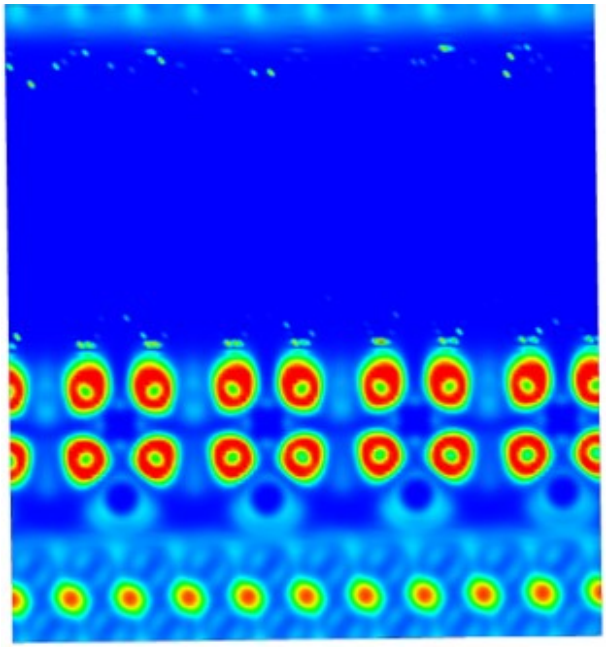

Fig. S8 (a) The electron localization function of the Fe_2N with (a) and without (b) the Fe_3O_4.

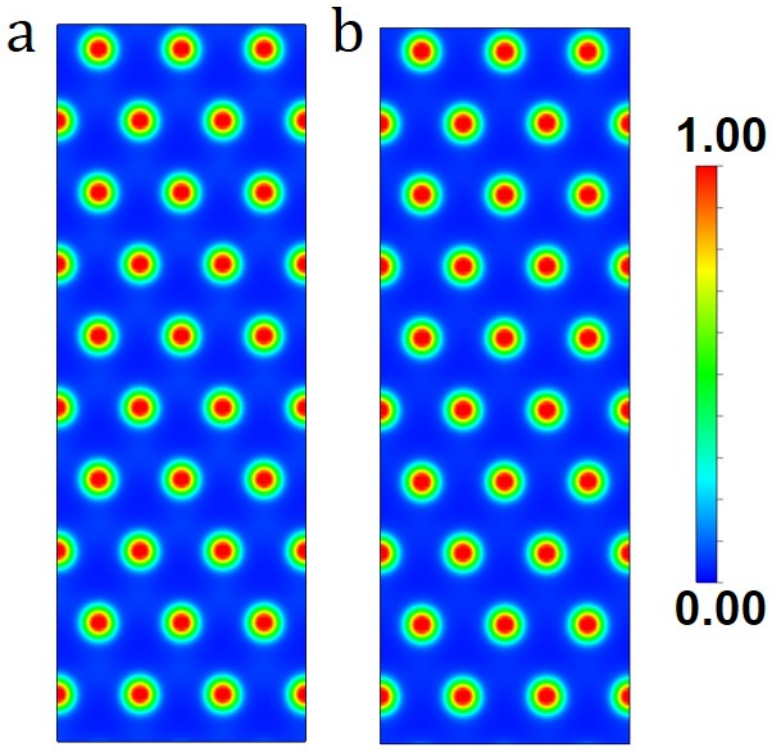

Fig. S9 The average Bader charge of the Fe_3O_4 (a), Fe_2N (b), and Fe_3O_4/Fe_2N (c).

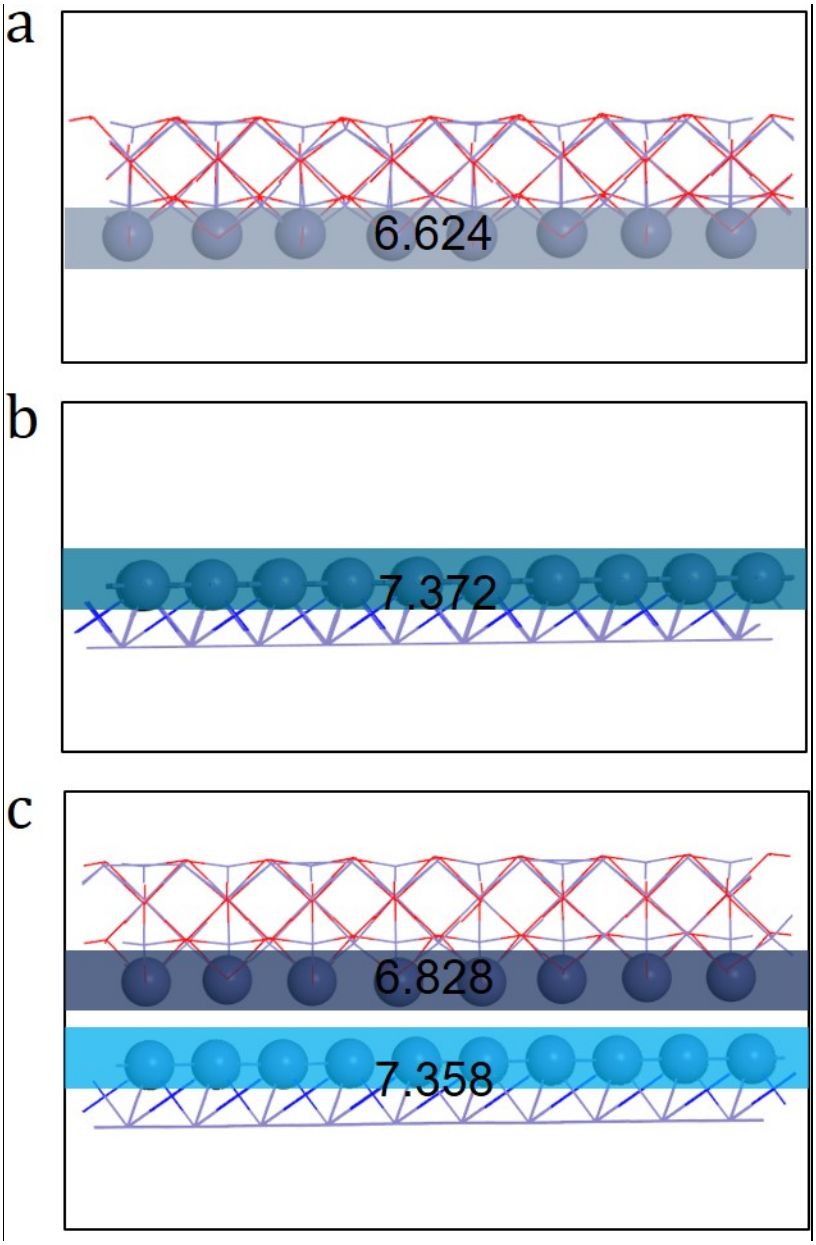

Fig. S10 The adsorption structure and adsorption energy of Li^+ on the (a) Fe_2O_3 and (b) Fe_3O_4/Fe_2N nano-heterojunctions, respectively.

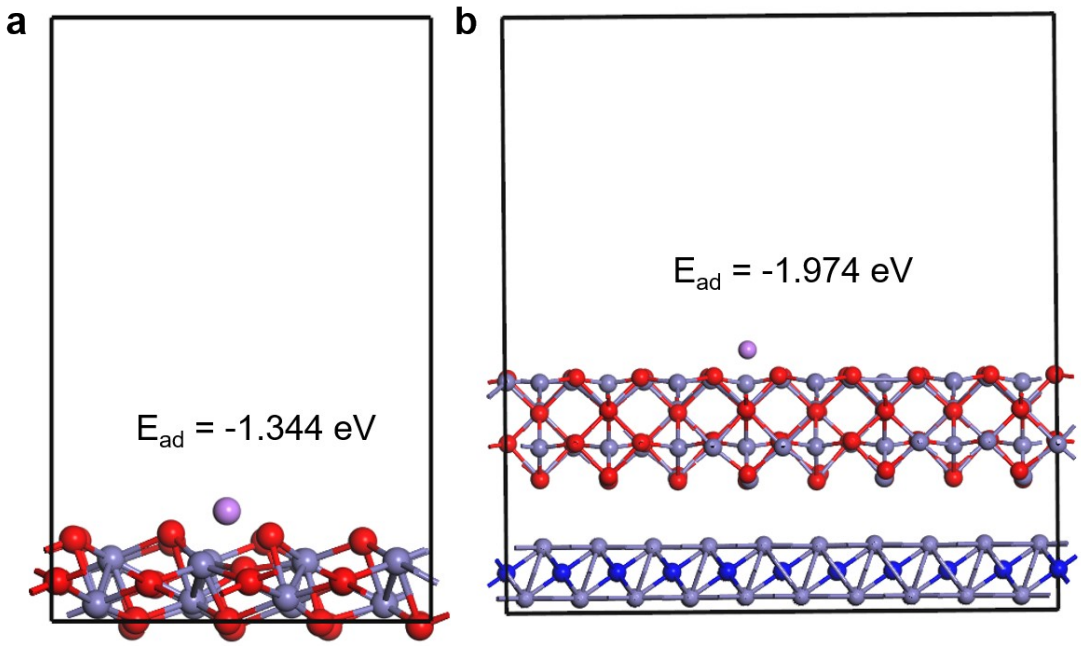

Fig. S11 (a, c, e, and g) CV curves of the Fe_2O_3, Fe_3O_4/Fe_2N-30, Fe_3O_4/Fe_2N-60 and Fe_2N electrodes at different scan rates, respectively. (b, d, f, and h) CV response of the Fe_2O_3, Fe_3O_4/Fe_2N-30, Fe_3O_4/Fe_2N-60, and Fe_2N electrodes at 1.0 mV s^{-1}, respectively.

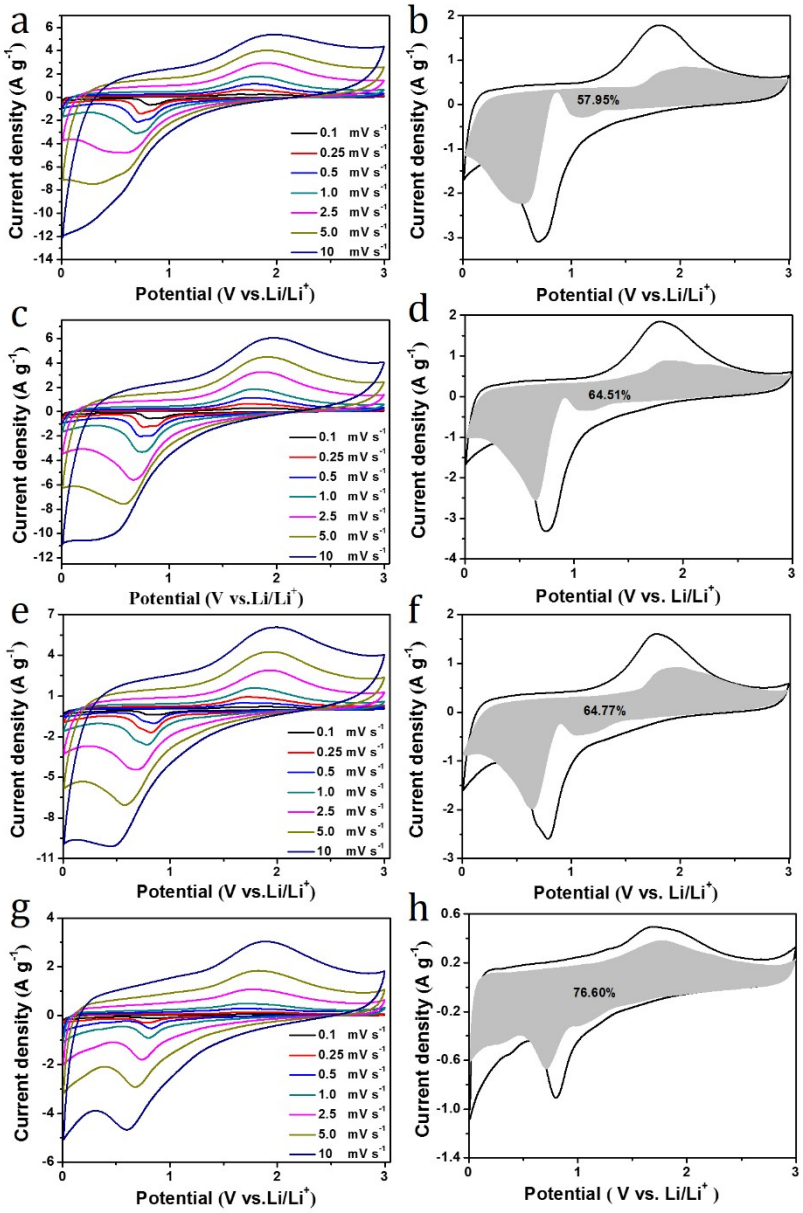

Fig. S12 (a) Discharge-charge curves of the GITT test. (b) Detailed voltage response during a single current pulse.

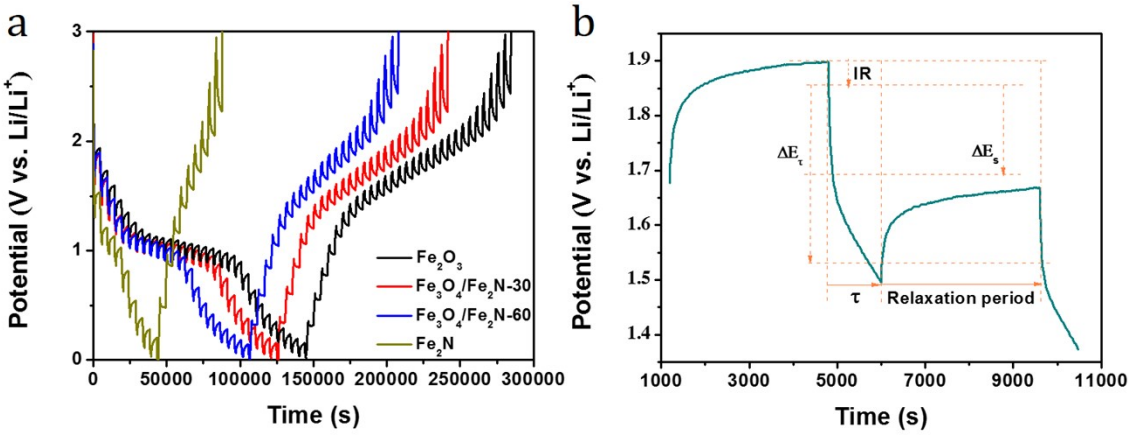

Fig. S13 Electrochemical characterizations of Nb-based samples. (a) The initial four integrated CV curves of $Nb_{12}O_{29}/Nb_4N_5$-15 nano-heterojunction at 0.1 mV s^{-1}. (b) The first four GCD profiles of $Nb_{12}O_{29}/Nb_4N_5$-15 nano-heterojunction at 0.1 A g^{-1}. (c) Integrated CV curves at 0.1 mV s^{-1}. (d) *b* value determination. (e) Capacitive contribution in CV curves at different scan rates.

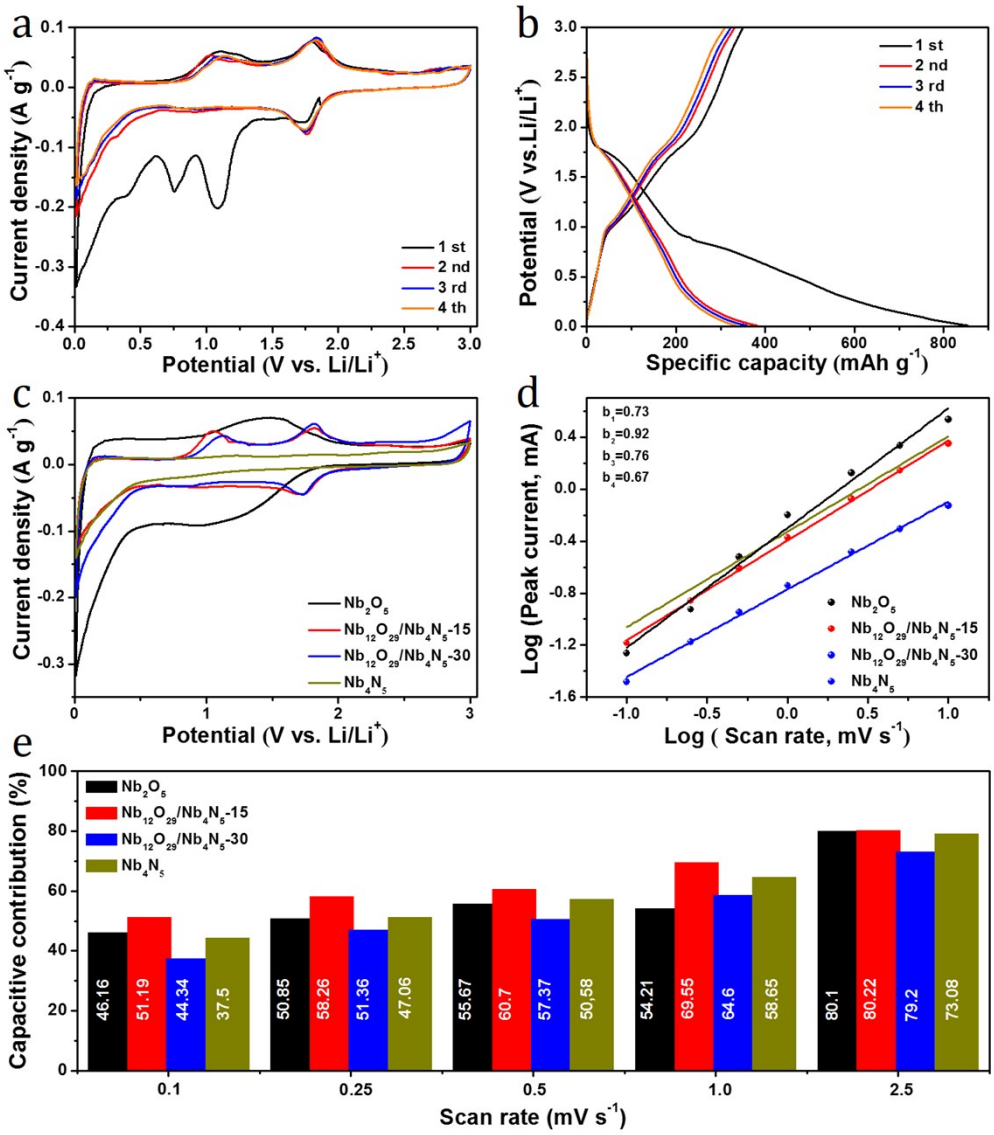

Fig. S14 (a, c, e, and f) CV curves of Nb_2O_5, $Nb_{12}O_{29}/Nb_4N_5$-15, $Nb_{12}O_{29}/Nb_4N_5$-30, and Nb_4N_5 electrodes at different scan rates, respectively. (b, d, f, and h) CV response of Nb_2O_5, $Nb_{12}O_{29}/Nb_4N_5$-15， $Nb_{12}O_{29}/Nb_4N_5$-30, and Nb_4N_5 electrodes at 1.0 mV s^{-1}, respectively.

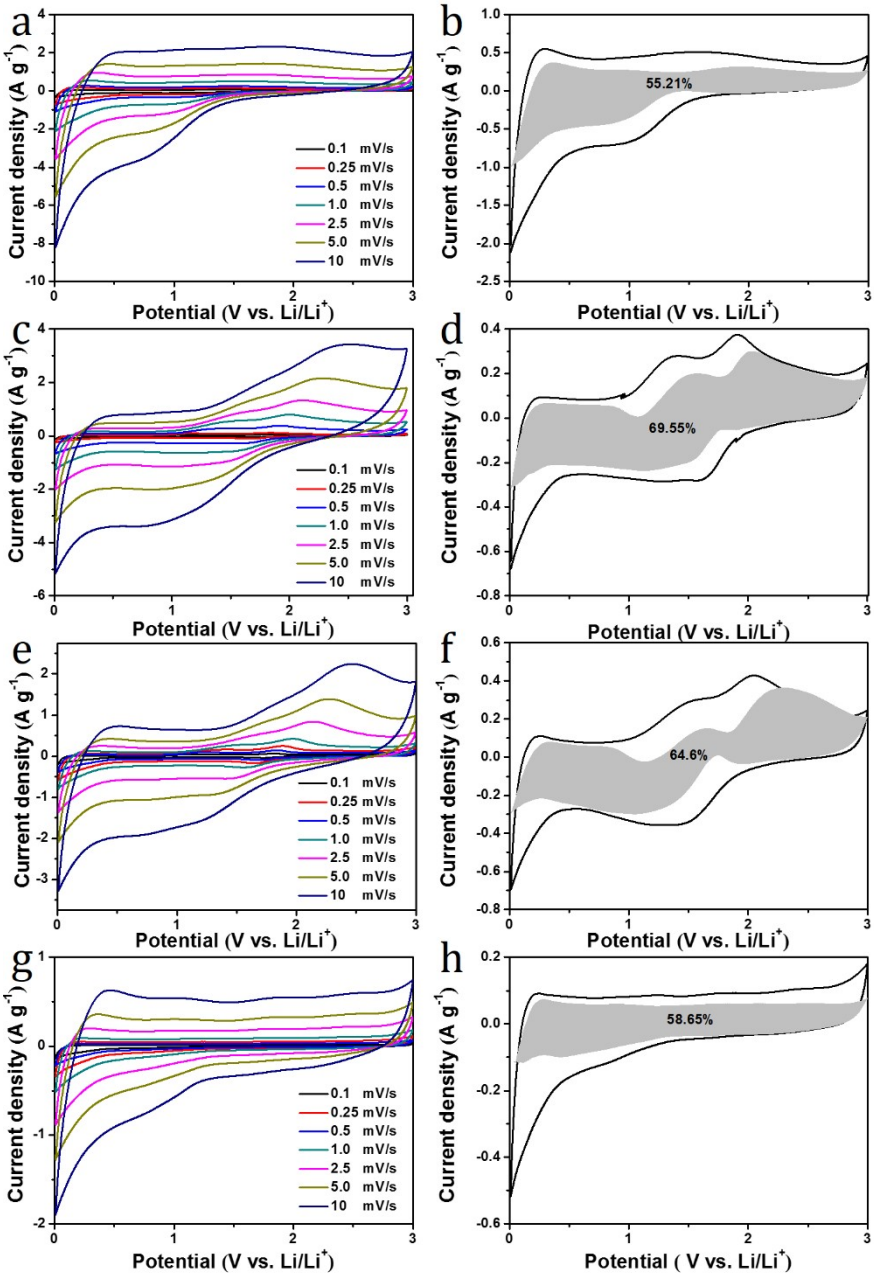

Fig. S15 Kinetic analysis of the Li^+ storage behavior of Nb-based samples. (a) Nyquist plots. (b) The Warburg value. (c) Discharge-charge curves of the GITT test. (d) Lithium-ion diffusion coefficient as a function of discharge process (d) and charge process (e). (f) Rate capability. (g) Cycling performance with the corresponding Coulombic efficiency at 1.0 A g^{-1}.

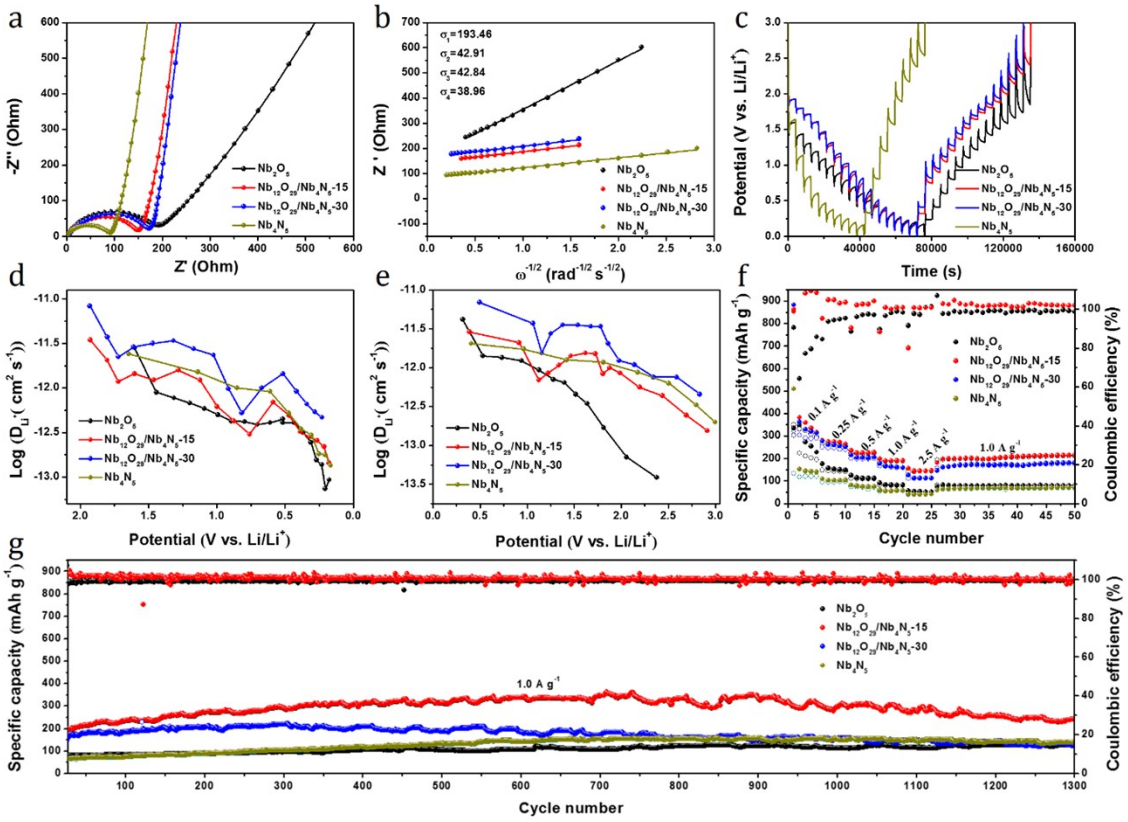

Fig. S16 Electrochemical characterizations of W-based samples. (a) The initial five integrated CV curves of $WO_{2.92}$/WN-30 nano-heterojunction at 0.1 mV s^{-1}. (b) The first five GCD profiles of $WO_{2.92}$/WN-30 nano-heterojunction at 0.1 A g^{-1}. (c) Integrated CV curves at 0.1 mV s^{-1}. (d) *b* value determination. (e) Capacitive contribution in CV curves at different scan rates.

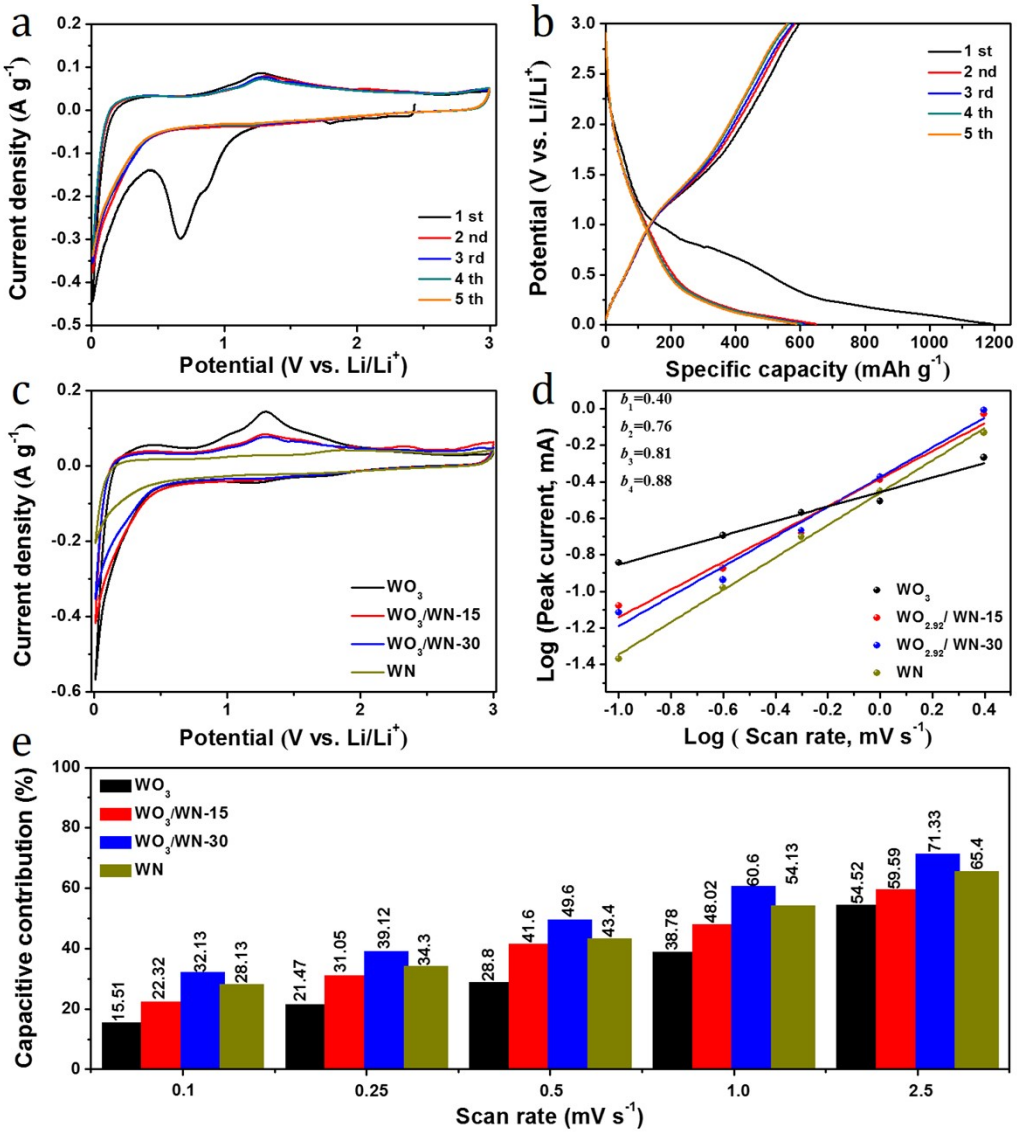

Fig. S17 (a, c, e, and g) CV curves of WO_3, $WO_{2.92}$/WN-15, $WO_{2.92}$/WN-30, and WN electrodes at different scan rates, respectively. (b, d, f, and h) CV response of WO_3, $WO_{2.92}$/WN-15, $WO_{2.92}$/WN-30, and WN electrodes at a scan rate of 1.0 mV s^{-1}, respectively.

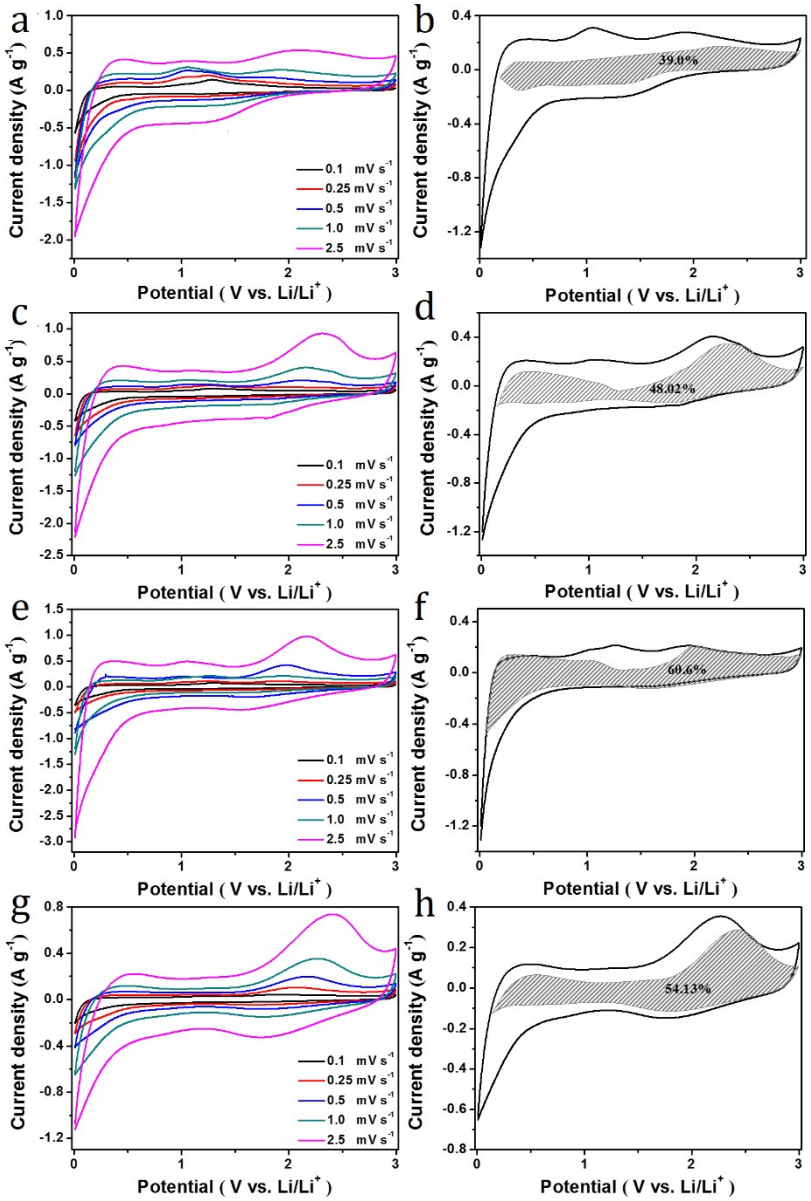

Fig. S18 Kinetic analysis of the Li^+ storage behavior of W-based samples. (a) Nyquist plots. (b) The Warburg value. (c) Discharge-charge curves of the GITT test. (d) Lithium-ion diffusion coefficient as a function of discharge process (d) and charge process (e). (f) Rate capability. (g) Cycling performance with the corresponding Coulombic efficiency at 1.0 A g^{-1}.

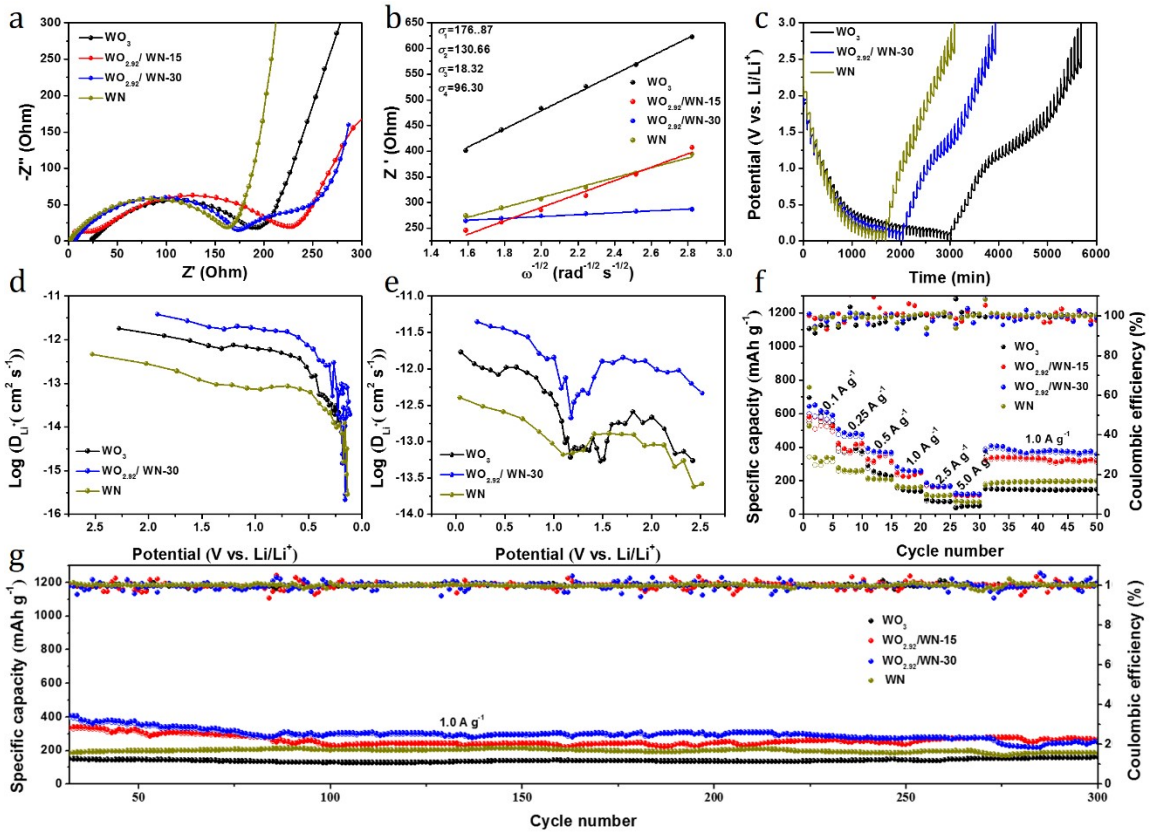

Table S2 The equivalent electrical circuit model used for fitting the Nyquist plots and the values derived from the fitted data.

Samples	**Fe_2O_3**	**Fe_3O_4/Fe_2N-30**	**Fe_3O_4/Fe_2N-60**	**Fe_2N**
Equivalent Circuit	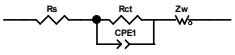	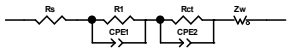	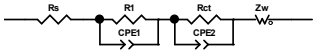	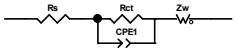
R_{ct} (Ω)	227.21	184.7	145.1	132.6
σ (Ω $S^{-1/2}$)	50.27	51.57	42.96	35.12
Samples	**Nb_2O_5**	**$Nb_{12}O_{29}/Nb_4N_5$-15**	**$Nb_{12}O_{29}/Nb_4N_5$-30**	**Nb_4N_5**
Equivalent Circuit	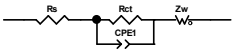	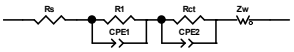	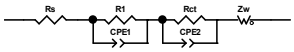	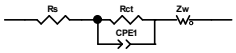
R_{ct} (Ω)	193.3	173.2	150	91.6
σ (Ω $S^{-1/2}$)	193.46	42.91	42.81	38.96
Samples	**WO_3**	**$WO_{2.92}/WN$-15**	**$WO_{2.92}/WN$-30**	**WN**
Equivalent Circuit	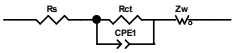	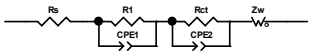	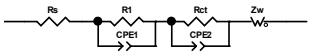	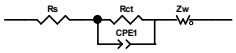
R_{ct} (Ω)	228.7	194.4	174.8	161.9
σ (Ω $S^{-1/2}$)	176.55	130.76	42.83	38.96

Table S3 The comparison of the electrochemical performance of the nano-heterojunctions with their individuals.

Samples	Fe_2O_3	Fe_3O_4/Fe_2N-30	Fe_3O_4/Fe_2N-60	Fe_2N
Specific Capacity at 0.1 A g^{-1} (mAh g^{-1})	1231.9	984.3	712.3	115.2
Rate Capability at 2.5 A g^{-1} (mAh g^{-1})	680.8	398.5	531.3	49.7
Samples	**Nb_2O_5**	**$Nb_{12}O_{29}/Nb_4N_5$-15**	**$Nb_{12}O_{29}/Nb_4N_5$-30**	**Nb_4N_5**
Specific Capacity at 0.1 A g^{-1} (mAh g^{-1})	303.5	350.2	323.8	133.7
Rate Capability at 2.5 A g^{-1} (mAh g^{-1})	52.0	142.0	113.3	40.4
Samples	**WO_3**	**$WO_{2.92}$/WN-15**	**$WO_{2.92}$/WN-30**	**WN**
Specific Capacity at 0.1 A g^{-1} (mAh g^{-1})	545.2	561.7	462.3	407.0
Rate Capability at 5.0 A g^{-1} (mAh g^{-1})	50.5	111.5	119.6	60.0